

Triazole-functionalized Ni-MOF-74 for high-performance CO₂ capture: Balancing capacity, selectivity, and humidity tolerance

Shuo Gao ^a, Wanru Feng ^a, Junsu Jin ^{a,*}, Jianguo Mi ^a, Hong Meng ^{b,*}

^a Beijing Key Laboratory of Membrane Science and Technology, Beijing University of Chemical Technology, Beijing 100029, China

^b Xinjiang University, Urumqi 830046, China

ARTICLE INFO

Keywords:
MOF functionalization
CO₂ adsorption
CO₂/N₂ selectivity
High humidity
Stability

ABSTRACT

We present a strategy to design moisture-resistant MOFs with balanced CO₂ capture performance by integrating triazole derivatives into the Ni-MOF-74 framework. Among the modified materials, Ni-Datz-MOF-74, functionalized with 3,5-diamino-1,2,4-triazole, exhibits exceptional CO₂ uptake capacities of 4.71 and 3.93 mmol g⁻¹ at 298 and 313 K (0.15 bar), corresponding to 1.98- and 2.39-fold enhancements over pristine Ni-MOF-74, respectively. Ni-Datz-MOF-74 achieves an impressive IAST selectivity of 327 for CO₂/N₂ (298 K, 15:85, v/v), which is 11 times higher than the Ni-MOF-74, and the dynamic CO₂ adsorption capacity and selectivity of Ni-Datz-MOF-74 (3.06 mmol g⁻¹, 171.7) were significantly higher than the Ni-MOF-74 (1.71 mmol g⁻¹, 66.3), which is in good agreement with the results predicted by the Ideal Adsorbed Solution Theory (IAST) under static conditions. Remarkably, under humid condition (80 % RH), Ni-Datz-MOF-74 demonstrates superior CO₂ capacity (3.28 mmol g⁻¹) compared to dry condition (3.06 mmol g⁻¹), attributed to the formation of bicarbonate species, as confirmed by in-situ IR spectroscopy. The Ni-Datz-MOF-74 also exhibits excellent stability, with only 4.1 % and 8.2 % capacity loss after 20 adsorption-desorption cycles and one week of water immersion at 353 K, respectively. DFT calculations further elucidate the critical role of amino groups in enhancing both adsorption capacity and gas selectivity. This work highlights Ni-Datz-MOF-74 as a promising and scalable material for industrial carbon capture, combining low moisture sensitivity with high adsorption performance and selectivity.

1. Introduction

In addressing global climate change driven by CO₂ emissions from extensive fossil fuel combustion and achieving carbon neutrality goals, carbon capture, utilization, and storage (CCUS) technologies are paramount [1]. Amine-based solvents and other absorbents have been widely adopted due to their high CO₂ absorption capacity and rapid absorption kinetics. However, they often lead to equipment corrosion, and issues such as oxidative degradation and ammonia volatilization can cause environmental contamination [2]. In this context, solid adsorbents based on physical adsorption have attracted significant research interest. Although traditional porous materials, such as activated carbon and zeolites are more environmentally friendly and exhibit lower adsorption energy consumption, their limited adsorption capacity and selectivity hinder their widespread application [3,4].

Metal-organic frameworks (MOFs), as a novel class of porous materials, have demonstrated remarkable potential in CO₂ capture owing to their high specific surface area, tunable pore sizes, and abundant open

metal sites [5–7]. Among various MOF materials, Ni-MOF-74 exhibits superior CO₂ adsorption performance owing to its abundant open metal sites, which serve as Lewis acids for strong polarization of gas adsorbates. By introducing diverse functional groups (–O–Li, –NH₂, –F, –CH₃) [8] and employing ligand substitution strategies [9], the CO₂ adsorption capabilities of Ni-MOF-74 can be further enhanced. However, the exposed unsaturated metal active sites readily bind with H₂O, thereby inhibiting CO₂ adsorption. Under high H₂O loading conditions (19.9 mmol g⁻¹, 78 % RH), the CO₂ adsorption capacity is significantly reduced to only 0.5 mmol g⁻¹ [10]. Additionally, the instability of Ni–O bonds renders the structure of Ni-MOF-74 susceptible to collapse upon exposure to water [11]. To the best of our knowledge, no studies have comprehensively addressed the simultaneous enhancement of CO₂ adsorption capacity, reduction of water sensitivity, and improvement of water stability in MOFs, enabling their application in high-humidity CO₂ capture scenarios.

Amine-grafted MCM-41 silica (MONO-PE-MCM-41) exhibits higher CO₂ adsorption capacity under humid conditions compared to dry

* Corresponding authors.

E-mail addresses: jinjs@buct.edu.cn (J. Jin), menghong@xju.edu.cn (H. Meng).

environments. This enhancement is attributed to the shift from carbamate to bicarbonate formation during adsorption, which alters the amine-to-CO₂ adsorption ratio from 2:1 to 1:1 [12]. Additionally, the dual-ligand synergy strategy represents an effective approach for structural modification. For instance, CALF-20, a water-stable MOF, is constructed by incorporating triazole into a Zn-oxalate framework, demonstrating structural stability even under 250 °C water vapor [13]. ZU-301 [14] owing to the hydrophobic effect of methyl groups, maintains a high dynamic CO₂ adsorption capacity (1.66 mmol g⁻¹) under humid condition, with only a 2.9 % reduction compared to its pristine form.

Inspired by the co-synergistic effect of water molecules (bicarbonate formation) in amine-grafted functionalization under humid condition and the high stability of triazole molecules, this study integrates four triazole derivatives into the Ni-MOF-74 framework. Remarkably, Ni-Datz-MOF-74, functionalized with 3,5-diamino-1,2,4-triazole as a secondary ligand, exhibits exceptional CO₂ adsorption capacity and high selectivity under both static and dynamic conditions, whether dry or humid (15 % CO₂, 85 % N₂, 80 % RH). Furthermore, the crystal structure of Ni-Datz-MOF-74 remains highly stable after 20 consecutive adsorption-desorption cycles and prolonged immersion in high-temperature water. This work presents a novel strategy for designing MOF materials capable of long-term stable operation in high-humidity environments.

2. Experimental section

2.1. Materials

All chemicals were obtained from commercial sources and used without further purification: nickel acetate (TCI, 99.9 %), 3-methyl-1,2,4-triazole (Mtz, Sigma-Aldrich, 98 %), Tetrahydrofuran (THF, Roth, 99.5 %), 2,5-dihydroxyterephthalic acid (Sigma-Aldrich, 98 %), anhydrous ethanol (Sigma-Aldrich, 99.7 %), 3-amino-1,2,4-triazole (Atz, Sigma-Aldrich, 96 %), 3,5-diamino-1,2,4-triazole (Datz, Sigma-Aldrich, 98 %), and 3,5-dimethyl-1,2,4-triazole (Dmtz, Sigma-Aldrich, 95 %).

2.2. Synthesis of Ni-MOF-74 and modified samples

The Ni-MOF-74 and modified samples used in this work were synthesized by hydrothermal method as described in Supporting information (S1).

2.3. Characterization of Ni-MOF-74 and modified samples

The structural properties of the materials were analyzed and characterized using techniques such as Scanning electron microscopy (SEM), X-ray diffraction (XRD), Fourier-transform infrared (FT-IR) spectra, X-ray photoelectron spectroscopy (XPS), Thermogravimetric analysis (TGA), and the details of the steps and conditions are described in Supporting information (S2).

2.4. Experiment methods

The adsorption isotherm measurements, dynamic breakthrough experiments and In-situ FTIR of CO₂ (dry and humid) were carried out in this work, the details of the steps and conditions in each experiment, calculation methods, and formulas are described in Supporting information (S3–S7).

3. Results and discussion

3.1. Characterization of samples

Through solvothermal reactions, the high bond energy and low steric

hindrance of the N=N group facilitated the formation of new Ni-N bonds with Ni, successfully integrating the triazole into the MOF framework (Fig. 1a). The morphologies of the Ni-MOF-74 powder and modified samples were characterized using scanning electron microscopy (SEM). Prior to testing, the powders were dispersed in ethanol, dried, and coated with gold to enhance conductivity. The SEM images and energy-dispersive spectroscopy (EDS) mapping (Fig. S1) revealed that the synthesized materials exhibited a durian-like spherical morphology composed of blocky crystals with diameters ranging from 1 to 2 μm, indicating that the modifications did not significantly alter the sample morphology. Additionally, the EDS spectra clearly demonstrated that, except for the pristine Ni-MOF-74, the N element was uniformly distributed in all modified powder materials.

The XRD patterns (Fig. 1b) reveal that the samples exhibit two intense diffraction peaks at $2\theta = 6.8^\circ$ and 11.8° , corresponding to the (210) and (030) crystal planes, respectively. These peaks are in excellent agreement with the previously reported simulated XRD pattern of Ni-MOF-74 powder [15–17]. However, the diffraction peaks of the modified Ni-Datz-MOF-74 are sharper, indicating enhanced crystallinity. From the FT-IR spectra (Fig. 1c), the IR peak at 3415 cm⁻¹ arises from the unsaturated C-H bond vibration on the benzene ring of 2,5-dihydroxyterephthalic acid, while the peaks at 1557 and 1411 cm⁻¹ correspond to the stretching vibrations of the C=O and C=C bonds in 2,5-dihydroxyterephthalic acid, respectively [18]. The peaks observed at 888 and 825 cm⁻¹ are attributed to the out-of-plane bending vibrations of the benzene ring [19–21]. Notably, the characteristic peaks at 664, 1022, and 1291 cm⁻¹ are attributed to the vibrations of the N-C≡N, C-N, and N-H bonds on the triazole molecular ring [22], confirming the successful incorporation of triazole molecules into the Ni-MOF-74 framework.

Thermogravimetric analysis (TGA) was performed under a N₂ atmosphere (Fig. S2) to evaluate the thermal stability of the modified powders. The results indicate that the thermal decomposition of both the pristine and modified samples can be categorized into three stages. The initial mass loss below 313–373 K is attributed to the removal of free water and solvents from the pores [23]; The mass loss between 373 and 423 K corresponds to the elimination of guest molecules, such as water and residual solvents (Ethanol and THF), bound to the unsaturated Ni sites within the micropores [24], the third stage observed between 623 and 823 K is attributed to ligand decomposition and structural collapse [25]. Notably, Ni-Datz-MOF-74 exhibits excellent thermal stability between 423–660 K, making it suitable for most low- and medium-temperature CO₂ capture applications.

To investigate the changes in pore structure resulting from the insertion of triazole into the Ni-MOF-74 framework, we measured the specific surface area and pore structure of the samples using a surface area analyzer. N₂ adsorption–desorption isotherms were measured at 77 K, samples exhibited rapid N₂ adsorption at very low P/P₀ (<0.05), with a noticeable decrease in adsorption capacity as P/P₀ increased (0.9–1.0), consistent with Type I isotherms, confirming the microporous nature of the modified samples. The specific surface areas (micropore volumes) of Ni-MOF-74, Ni-Atz-MOF-74, Ni-Datz-MOF-74, Ni-Mtz-MOF-74, and Ni-Dmtz-MOF-74 (Fig. 1d) were 918.75 m² g⁻¹ (0.47 cm³ g⁻¹), 534.41 m² g⁻¹ (0.21 cm³ g⁻¹), 702.55 m² g⁻¹ (0.27 cm³ g⁻¹), 662.16 m² g⁻¹ (0.25 cm³ g⁻¹), and 474.46 m² g⁻¹ (0.18 cm³ g⁻¹), respectively. This reduction in the specific surface area of modified samples is attributed to the successful incorporation of the triazole framework into the structure. Additionally, the triazole molecules occupy space within the cavities, transforming larger pores into smaller ones (Fig. 1e), resulting in more ultramicro pores (0.37–0.5 nm) in the modified powders compared to the pristine sample. And the most probable pore sizes of the four modified MOFs follow this order: Ni-Datz-MOF-74 (0.38 nm) < Ni-Dmtz-MOF-74 (0.41 nm) < Ni-Mtz-MOF-74 (0.42 nm) < Ni-Atz-MOF-74 (0.45 nm). When adsorption occurs in extremely narrow channels, the overlapping potential fields from adjacent walls lead to significantly enhanced non-specific interactions. This intensified adsorption potential

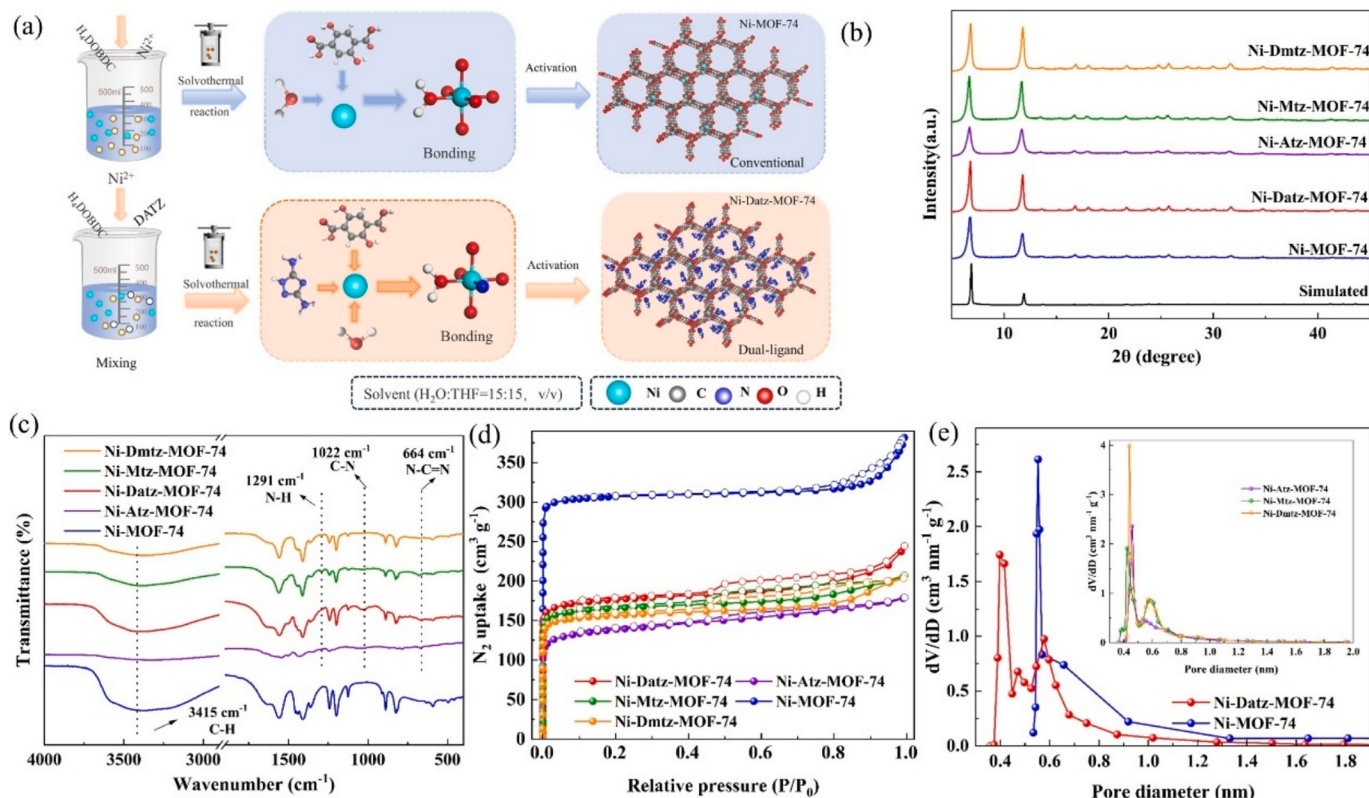


Fig. 1. (a) Schematic illustration of the preparation process for pristine Ni-MOF-74 and amino-rich Ni-Datz-MOF-74 modified powder, (b) XRD patterns, (c) FT-IR spectra, (d) N₂ adsorption-desorption isotherms at 77 K, and (e) Micropore size distribution calculated using the H-K method for Ni-MOF-74, Ni-Atz-MOF-74, Ni-Datz-MOF-74, Ni-Mtz-MOF-74, and Ni-Dmtz-MOF-74.

enables CO₂ to fill the ultramicropores of modified MOFs at relatively low pressures [26]. The narrowed pore size significantly enhances the molecular sieving effect (such as ZNU-9, ZNU-11 and CAU-10-Py), improving the separation selectivity for mixed gases [27–29].

We further investigated the chemical states of Ni-Datz-MOF-74 using X-ray photoelectron spectroscopy (XPS) wide-scan analysis. As shown in Fig. 2a, Ni-Datz-MOF-74 exhibits an additional N signal peak compared to Ni-MOF-74, which only displays C, Ni, and O peaks. In the high-resolution Ni 2p spectrum of Ni-Datz-MOF-74 (Fig. 2b), the Ni 2p region can be deconvoluted into six distinct peaks. The Ni 2p_{1/2} peaks at 873.75 eV, 877.45 eV, and 881.19 eV correspond to the Ni 2p_{3/2} peaks at 856.17 eV (Ni–O bond) [30], 860.30 eV (Ni–N bond) [31], and 863.60 eV (Ni–O satellite peak), respectively [32]. In contrast, Ni-MOF-74 exhibits two Ni 2p_{1/2} peaks at 874.26 eV and 879.58 eV, corresponding to the Ni 2p_{3/2} peaks at 856.80 eV (Ni–O bond) and 861.73 eV (satellite peak) [33,34]. The negative shift in the Ni–O peak position of Ni-Datz-MOF-

74 may result from N doping, which alters the electronic structure of the Ni center. Due to the higher electronegativity of N compared to Ni, some electrons originally contributing to O are transferred to N [35]. In the high-resolution N 1 s spectrum (Fig. 2c), the peaks at 399.50 eV and 400.38 eV are attributed to the formation of Ni–N and C–N bonds [36–38], further confirming the successful incorporation of triazole into the Ni-MOF-74 framework.

3.2. Gas adsorption experiments

The CO₂ and N₂ adsorption capacities of the synthesized MOF-74(Ni) materials were evaluated at 298 K (Fig. S4a–c). As shown in Fig. 3a–c, the modified powders exhibited higher CO₂ adsorption capacities compared to the pristine Ni-MOF-74. Notably, Ni-Datz-MOF-74 demonstrated a CO₂ adsorption capacity of 4.71 mmol g⁻¹ at 0.15 bar, representing a twofold increase over the pristine Ni-MOF-74 (2.38

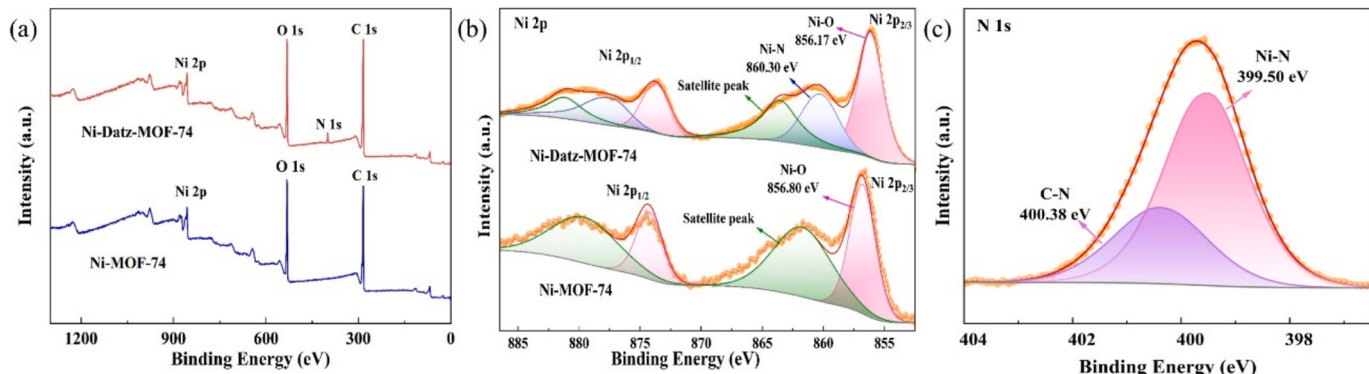


Fig. 2. XPS spectra of Ni-MOF-74 and Ni-Datz-MOF-74. (a) Full scan, (b) Ni 2p, (c) N 1s of Ni-Datz-MOF-74.

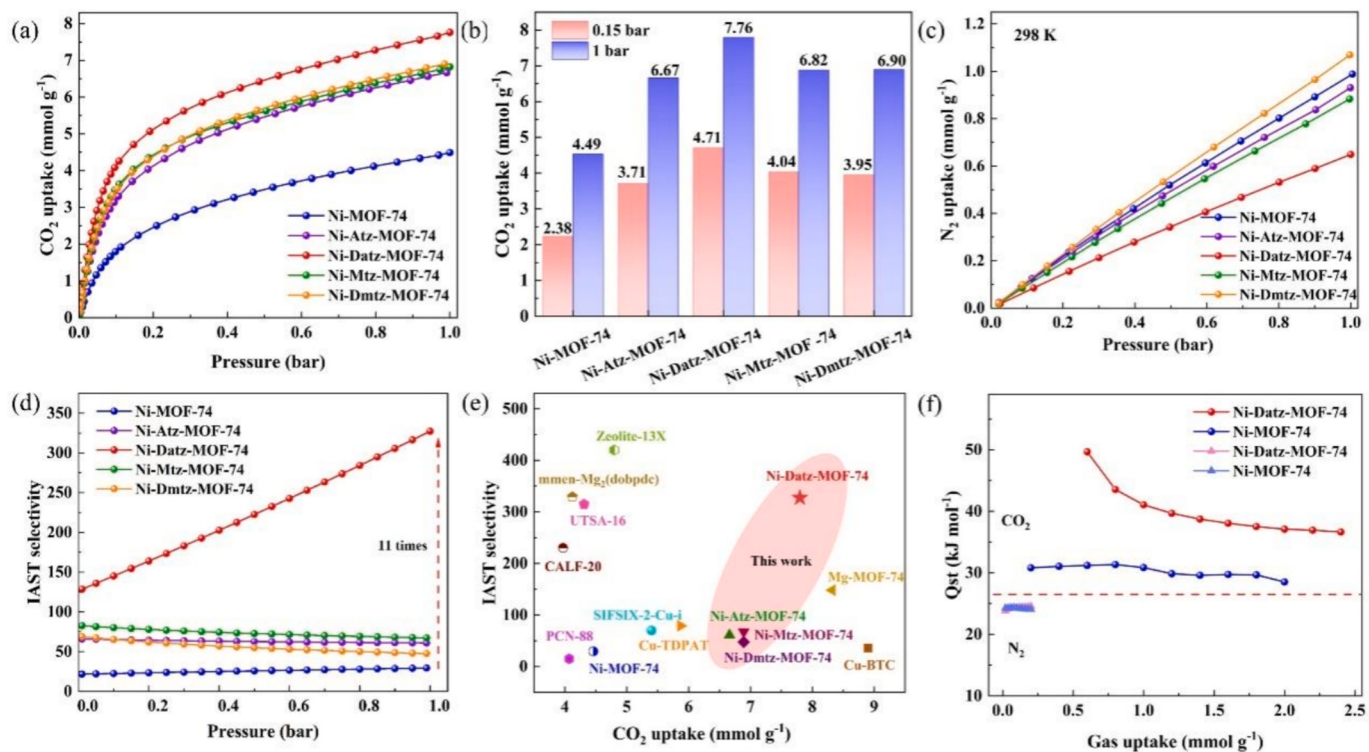


Fig. 3. Gas separation performance of samples. (a) CO₂ adsorption isotherms, (b) CO₂ adsorption capacities at 0.15 bar and 1 bar, (c) N₂ adsorption isotherms, (d) IAST selectivity for CO₂/N₂ (15/85, v/v) mixed gas, (e) comparison of IAST selectivity (CO₂/N₂, 15/85, v/v) with other MOFs exhibiting high CO₂ adsorption capacities, (f) adsorption heat.

mmol g⁻¹). At 1 bar, Ni-Datz-MOF-74 achieved the highest CO₂ adsorption capacity (7.76 mmol g⁻¹) and the lowest N₂ adsorption capacity (0.66 mmol g⁻¹), with its CO₂ uptake being 1.73 times that of the pristine sample (4.49 mmol g⁻¹). Furthermore, the CO₂ adsorption isotherms of Ni-Datz-MOF-74 from 273 to 333 K (Fig. S4f) revealed consistently high adsorption capacities across a wide temperature range. The significant enhancement in adsorption performance is attributed to the strong quadrupole interactions between CO₂ and the N atoms within the pores [39]. We employed the Dual-site Langmuir-Freundlich (DSLF) and Single-site Langmuir-Freundlich (SSLF) models to fit the CO₂ and N₂ adsorption data (Figs. S8–S9 and Tables S4–S5) and calculated the CO₂/N₂ separation selectivity using the Ideal Adsorbed Solution Theory (IAST). As shown in Fig. 3d, Ni-Datz-MOF-74 exhibits a CO₂/N₂ (15/85, v/v) selectivity of 327, which is 11 times that of the Ni-MOF-74 (29). Interestingly, the selectivity of Ni-Datz-MOF-74 increases with higher CO₂ loading, likely due to the smaller kinetic diameter of CO₂ (3.30 Å) compared to N₂ (3.64 Å) (Table S2), enabling CO₂ to preferentially enter and adsorb within the pores [40]. Competitive adsorption results in CO₂ occupying more active sites, significantly reducing the available sites for N₂ adsorption. Additionally, the narrowed pore size enhances the molecular sieving effect, restricting the entry and adsorption of N₂ molecules [41]. These factors are crucial for achieving a balance between high CO₂ adsorption capacity and superior CO₂/N₂ selectivity. As illustrated in Fig. 3e, Ni-Datz-MOF-74 demonstrates both exceptional CO₂ adsorption capacity and high CO₂/N₂ separation selectivity. While Ni-Datz-MOF-74 shows lower selectivity compared to benchmark MOF materials, such as Zn-ox-mtz (>10⁶, 298 K) [42] and NICS (>10³, 298 K) [43], compared to MOFs with either high adsorption capacity or high selectivity, Ni-Datz-MOF-74 exhibits a more balanced and comprehensive separation performance (Table S3), which is a critical criterion for practical industrial applications [44].

The isosteric heat of adsorption (Q_{st}) plays a pivotal role in energy consumption considerations in process design and in evaluating the strength of interactions between the modified materials and adsorbates.

Using CO₂ and N₂ adsorption isotherms at three different temperatures, the Q_{st} values were calculated by applying the Clausius-Clapeyron equation to ten defined adsorption quantities [45]. The calculated results are presented in Fig. 3f (details are provided in Figs. S10–S11). The CO₂ adsorption heat of Ni-Datz-MOF-74 (34.7–49.7 kJ mol⁻¹) is significantly higher than that of the pristine Ni-MOF-74 (18.6–31.3 kJ mol⁻¹), unequivocally demonstrating the enhanced CO₂ affinity resulting from triazole incorporation. Additionally, the CO₂ adsorption heat of Ni-Datz-MOF-74 is much higher than its N₂ adsorption heat (23.8–24.6 kJ mol⁻¹), further confirming its high selectivity for CO₂ over N₂. Importantly, the adsorption heat of Ni-Datz-MOF-74 is well-positioned within the ideal range of 35–50 kJ mol⁻¹ for CO₂ capture from industrial flue gases, indicating its advantage in requiring relatively low desorption energy. This makes it highly promising for practical industrial applications.

3.3. Stability of Ni-Datz-MOF-74

Although MOFs exhibit considerable potential in gas separation applications, most suffer from poor cycling stability and structural collapse under humid and high-temperature conditions. Consequently, we performed 20 consecutive adsorption–desorption cycles on Ni-Datz-MOF-74, where each cycle involved CO₂ adsorption to saturation at 298 K followed by vacuum desorption at 433 K for 2 h. After 20 cycles, the CO₂ adsorption capacity of Ni-Datz-MOF-74 decreased by merely 4.1% (Fig. 4a), and SEM images confirmed that the structure remained intact without collapse (Fig. S3a–b). This underscores its excellent cycling and structural stability. Furthermore, we evaluated the hydrothermal stability of Ni-Datz-MOF-74 and Ni-MOF-74. Hydrothermal stability tests were conducted in a water environment at 313 K and 353 K. As shown in Fig. 4b, the CO₂ adsorption capacity of Ni-Datz-MOF-74 did not change obviously after being immersed in hot water at both temperatures for one day, and the CO₂ adsorption capacity of Ni-Datz-MOF-74 decreased by merely 8.2% (0.65 mmol g⁻¹) after one week of immersion at 353 K.

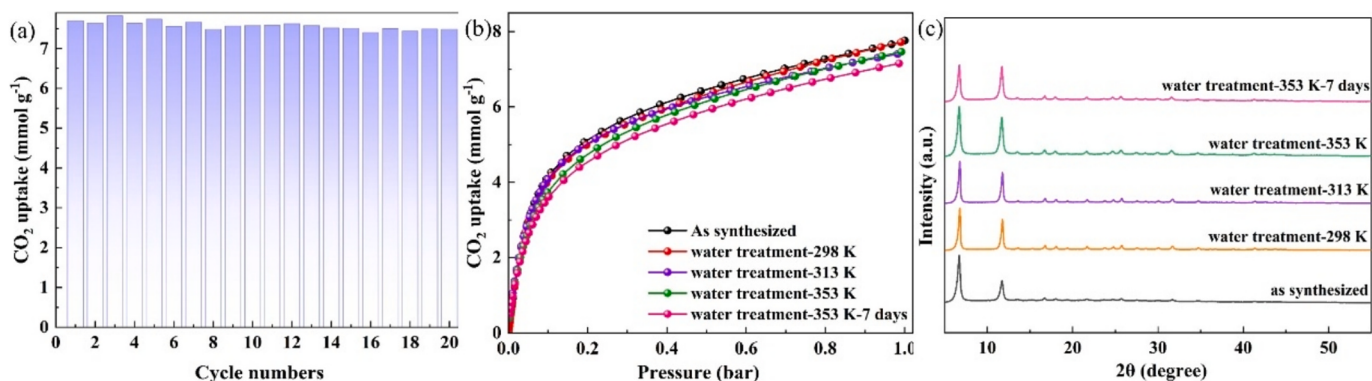


Fig. 4. (a) CO₂ cycling performance of Ni-Datz-MOF-74 (1 bar, 298 K), (b) CO₂ adsorption isotherms and (c) XRD patterns of Ni-Datz-MOF-74 after water treatment at different temperatures.

In contrast, TIFSIX-3-Ni, which also exhibits high CO₂ adsorption capacity, suffered a 40 % reduction in adsorption performance after immersion in water at 353 K for 24 h; NbOFFIVE-1-Ni showed a 25 % decrease in CO₂ uptake under identical hydrothermal conditions, and likewise, AlFFIVE-1-N failed to maintain structural stability in high-temperature aqueous environments [46]. The XRD pattern of Ni-Datz-MOF-74 after 7 days of immersion at 353 K remained virtually identical to that of the untreated sample, the slight enhancement in peak intensity following water immersion is attributed to the removal of impurities, which improves the diffraction intensity from crystalline planes [47]. SEM images (Fig. S3c-d) confirmed that its framework remained intact without damage from high-temperature water exposure. The notable improvement in hydrothermal stability is primarily attributed to the incorporation of the triazole framework, which substitutes some Ni-O bonds with Ni-N bonds, thereby reducing water

molecule attacks on Ni-O bonds and thereby enhancing the hydrothermal stability [48,49]. Although the water stability of Ni-Datz-MOF-74 is slightly inferior to that of some well-known MOF materials, such as UIO-66 [50] (after 12 months of aging in water still stable), BSF-1 (after 1 month in water still stable) [51], ZIF-68, 69, and 70 [52] (after seven days in boiling water still stable), their CO₂ adsorption capacity and mixed-gas separation selectivity are weaker than those of Ni-Datz-MOF-74. Therefore, while learning from and integrating the advantages of these highly water-stable MOF materials, it is crucial to develop MOFs with more balanced separation performance. Furthermore, to verify the reproducibility of this material, nine batches of samples (labeled 1–9) were prepared under identical experimental conditions, along with one scaled-up synthesis (No. 10, 8-fold scale). The adsorption isotherms of these ten batches were measured (Fig. S13). The results demonstrate minimal variation in CO₂ adsorption capacity (7.53–7.80 mmol g⁻¹,

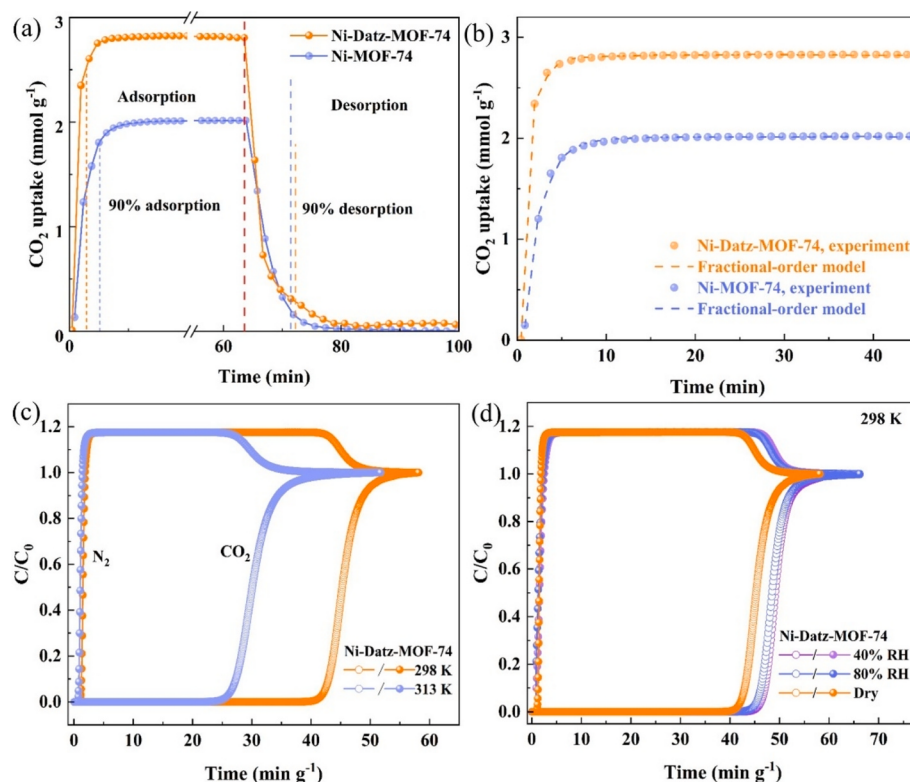


Fig. 5. (a) CO₂ (15 vol%) adsorption kinetic curves and (b) adsorption kinetic fitting based on the Fractional-order kinetic model of Ni-MOF-74 and Ni-Datz-MOF-74 at 298 K, (c) breakthrough curves of Ni-Datz-MOF-74 for CO₂/N₂ (15/85, v/v) under dry conditions (298 and 313 K), (d) breakthrough curves of Ni-Datz-MOF-74 for CO₂/N₂ (15/85, v/v) under dry and humid (40 % RH and 80 % RH) conditions at 298 K.

with only a 3 % difference), effectively confirming the excellent reproducibility of Ni-Datz-MOF-74. The yield of the scaled-up synthesis (13.89 g, 50.14 % yield) showed comparable results to the small-scale preparation (1.698 g, 50.28 % yield), further demonstrating its scalability. The production cost was calculated as shown in the table below, indicating that the raw material cost for preparing 1 g of Ni-Datz-MOF-74 powder is 2.486 \$. The prices of major raw materials are summarized in Table S7.

3.4. CO_2 kinetics and dynamic breakthrough experiments

In practical applications, rapid CO_2 adsorption kinetics serve as a critical parameter for evaluating adsorbent efficiency and play a significant role in continuous adsorption-separation processes. This study investigates the dynamic adsorption behavior of Ni-Datz-MOF-74 and Ni-MOF-74 using a gravimetric vapor sorption analyzer. The kinetic curves (Fig. 5a) show that the CO_2 adsorption capacity increases rapidly during the adsorption phase and reaches equilibrium promptly. Ni-Datz-MOF-74 and Ni-MOF-74 achieve 90 % of their equilibrium CO_2 adsorption capacities in 2.90 and 5.14 min, respectively, and reach 90 % desorption in 8.75 and 7.27 min, respectively. This indicates that Ni-Datz-MOF-74 exhibits faster adsorption kinetics than Ni-MOF-74, although its desorption rate is slightly slower due to the stronger CO_2 interactions facilitated by the amino groups. Three kinetic models were used to fit the adsorption process. While the Pseudo-first-order and Pseudo-second-order models tend to overestimate the initial and equilibrium stages of CO_2 adsorption, respectively, Ni-MOF-74 aligns better with the Pseudo-first-order model (Fig. S12, Table S6). Therefore, the Fractional-order model, which is applicable across a wide range of CO_2 adsorption capacities, was employed for fitting (Fig. 5b). The high R^2 value of 0.9996 for Ni-Datz-MOF-74 suggests its ability to describe complex reaction pathways [53,54]. Moreover, the rate constant of Ni-Datz-MOF-74 (0.21 min^{-1}) is significantly higher than that of Ni-MOF-74 (0.13 min^{-1}), indicating faster kinetics for the modified powder. This advantage is likely attributed to the stronger intermolecular interactions between CO_2 and the amino groups in the inserted triazole framework.

Subsequently, to further investigate the working capability of the modified materials in actual flue gas environments, dynamic breakthrough experiments were conducted under both humid and dry conditions using a CO_2/N_2 (15/85, v/v) mixed gas flow at 10 ml min^{-1} . Under dry conditions, Ni-Datz-MOF-74 exhibited CO_2 breakthrough times of 29.73 and 21.16 min g^{-1} at 298 and 313 K (Fig. 5c), respectively, with corresponding dynamic CO_2 adsorption capacities of 3.06 and 2.07 mmol g^{-1} . Although the reduction in CO_2 adsorption capacity of Ni-Datz-MOF-74 (32.36 %) was slightly higher than that of TIFSIX-Cu-TPA (35.4 %, from 298 to 328 K) [55] over a wide temperature range, lower than that of the high-performance dptz-CuTiF₆ (51.5 %, from 298 to 323 K) [56]. Notably, the dynamic selectivity of Ni-Datz-MOF-74 at 298 K reached 171.7, far surpassing that of other high- CO_2 -capacity MOFs such as Cu-BTC (15) [57]. In contrast, Ni-MOF-74 showed CO_2 breakthrough times of 17.53 and 8.26 min g^{-1} at 298 and 313 K, respectively, with corresponding CO_2 adsorption capacities of only 1.7 and 1.2 mmol g^{-1} (Fig. S5a, Table S1), significantly lower than those of Ni-Datz-MOF-74. Remarkably, under humid condition (Fig. 5d), the CO_2 breakthrough time of Ni-Datz-MOF-74 increased from 29.73 to 39.75 (40 % RH) and 38.37 min g^{-1} (80 % RH), with CO_2 adsorption capacities rising from 3.06 to 3.37 and 3.28 mmol g^{-1} , respectively. Furthermore, since Ni-Datz-MOF-74 exhibits significantly stronger interactions with CO_2 than with N_2 , CO_2 gradually displaces the adsorbed N_2 after the dry breakthrough point (Fig. S5c). Upon introduction of water vapor (Fig. S5d), competitive adsorption between H_2O and CO_2 molecules weakens this displacement effect, leading to increased N_2 uptake in both Ni-Datz-MOF-74 and Ni-MOF-74, consequently reducing their selectivity. Notably, the two materials possess distinct pore structures, that is Ni-Datz-MOF-74 has smaller pores (0.38

nm) compared to Ni-MOF-74 (0.60 nm), resulting in slightly more pronounced water vapor effects on Ni-Datz-MOF-74 [58,59]. In contrast, Ni-MOF-74 exhibited a 35.9 % decrease in CO_2 breakthrough time (from 17.53 to 11.24 min g^{-1}) under high humidity (80 % RH) (Fig. S5b). The reduced breakthrough time for Ni-MOF-74 is due to the competitive adsorption between H_2O and CO_2 molecules for available active sites. In contrast, the enhanced CO_2 adsorption capacity of Ni-Datz-MOF-74 under humid condition is due to the formation of bicarbonate/carbamate species in the presence of water, where the amino-to- CO_2 ratio is 1:1, compared to the 1:2 ratio in dry condition, where CO_2 absorption occurs via carbamate formation [60,61].

In situ infrared spectroscopy was used for continuous monitoring under dry and humid conditions to analyze the effect of water vapor on CO_2 adsorption by Ni-MOF-74 and Ni-Datz-MOF-74. The strong absorption band observed near 2360 cm^{-1} is attributed to the asymmetric stretching mode (v_3) of CO_2 , while the bands at 3600 and 3700 cm^{-1} correspond to the combination modes $v_3 + 2v_2$ and $v_3 + v_1$ of CO_2 , resulting from strong Fermi resonance effects [62].

For Ni-Datz-MOF-74 under dry condition, the band at 2360 cm^{-1} became prominent at 4 min, and the bands at 3600 and 3700 cm^{-1} appeared clearly between 8 and 10 min (Fig. 6a). Remarkably, under humid condition (80 % RH), the bands around 2360 , 3600 , and 3700 cm^{-1} emerged as early as 2 min (Fig. 6b). In contrast, for Ni-MOF-74 under dry condition, the band at 2360 cm^{-1} only began to appear at 6 min (Fig. S6a), and its emergence was further delayed to 8 min after the introduction of water vapor. Additionally, due to the competitive interference of water vapor, the band intensity started to decline at 30 min (Fig. S6b). The earlier appearance of spectral bands for Ni-Datz-MOF-74 under humid condition indicates that water vapor enhances its interaction with CO_2 , corroborating the breakthrough test results and highlighting the positive role of new active sites formed by pendant amino groups in the presence of water molecules for CO_2 adsorption. By narrowing the wavelength range, we can clearly observe the characteristic peaks corresponding to bicarbonate and carbamate formation as shown in Fig. 6c and Fig. S7. The strong peak observed at 1425 cm^{-1} is attributed to the symmetric C—O stretching of HCO_3^- [63,64]. The formation of the bicarbonate band indicates that bicarbonate species are generated on Ni-Datz-MOF-74 during CO_2 adsorption under 80 % humidity. Additionally, the peaks observed within the broad band at 1513 – 1556 cm^{-1} are associated with bond vibrations in carbamate species. For instance, the peaks at 1522 cm^{-1} arise from C-N bond formation, while those at 1540 cm^{-1} correspond to COO[−] stretching in carbamate [65].

3.5. Molecular simulations

To further investigate the enhanced CO_2/N_2 separation performance of Ni-Datz-MOF-74 over Ni-MOF-74, we employed density functional theory (DFT) to calculate the adsorption energies of both gases, exploring the interactions between the modified material, pristine material, and adsorbates (see computational details in S9). After incorporating the amino-triazole framework, the formation of Ni—N bonds created polar pore walls, which altered the interaction strength between Ni metal sites and adsorbates. Additionally, the pendant amino groups in the pores, with their H atoms acting as hydrogen bond donors, can form hydrogen bonds with the highly electronegative O atoms of CO_2 molecules. The synergistic effect of amino and metal sites significantly enhances the affinity for CO_2 molecules [66–68]. As illustrated, the interaction distances in pristine Ni-MOF-74 are 2.330 \AA for Ni···O_{CO2} (Fig. 7a) and 2.479 \AA for Ni···N_{N2} (Fig. 7b). In Ni-Datz-MOF-74, due to the confined nanopores, the interaction distances are 2.386 \AA for Ni···O_{CO2} (Fig. 7c), 2.372 \AA for H_{Amino}···O_{CO2} (Fig. 7d), and 2.565 \AA for Ni···N_{N2} (Fig. 7e). Shorter interaction distances correspond to stronger interactions. This adsorption configuration results in binding energies of -0.640 and -0.310 eV for CO_2 and N_2 , respectively, at the Ni metal sites of Ni-Datz-MOF-74, and -0.670 eV for CO_2 at the amino sites. In

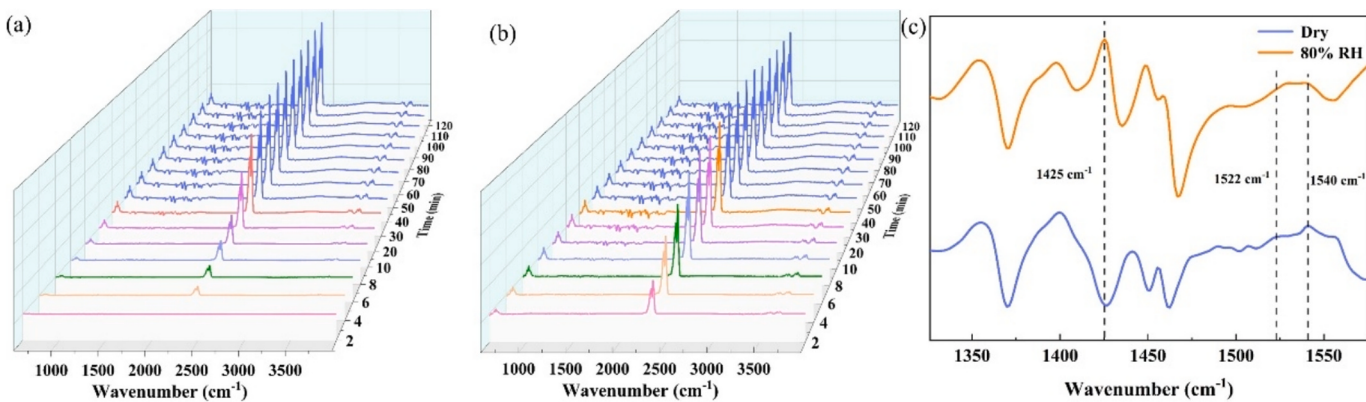


Fig. 6. In-situ IR spectra of (a) Ni-Datz-MOF-74 under dry and (b) humid (80% RH) condition (15/85, v/v); (c) comparison between dry and humid conditions within a narrow wavelength range.

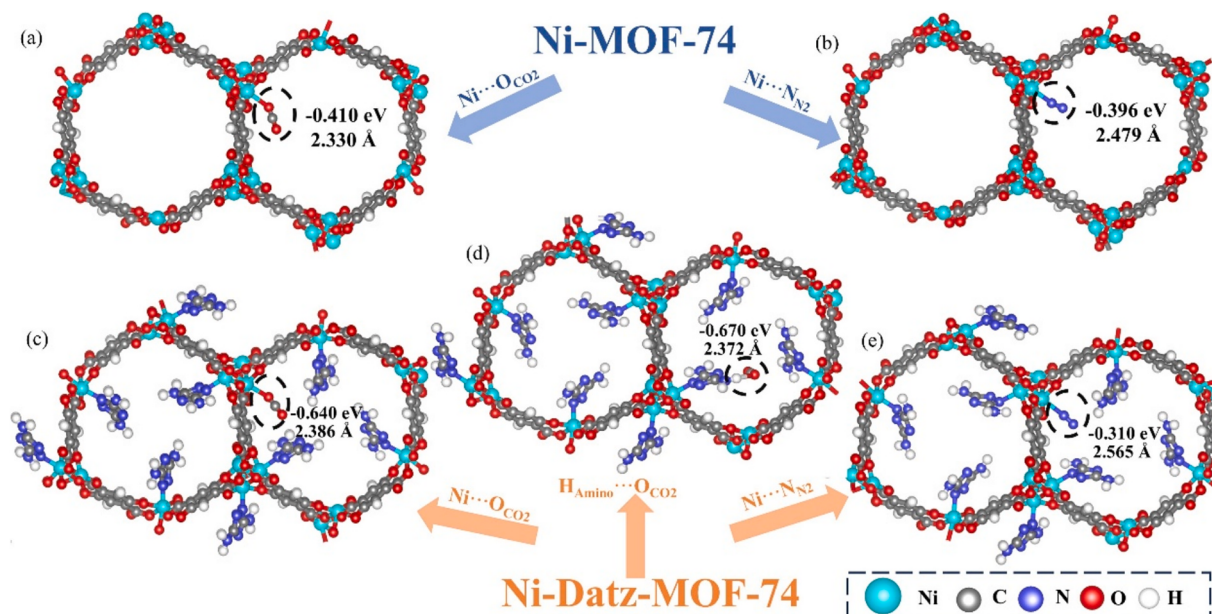


Fig. 7. DFT simulations reveal the adsorption energies and bonding distances between the Ni metal sites of Ni-MOF-74 with (a) CO₂ and (b) N₂, as well as between (c) Ni metal sites, (d) amino sites with CO₂, and (e) Ni metal sites with N₂ in Ni-Datz-MOF-74.

contrast, the binding energies for CO₂ and N₂ at the Ni metal sites of Ni-MOF-74 are -0.410 and -0.396 eV, respectively. The preferential bonding distances and the differences in binding energies before and after modification align well with the observed adsorption capacities and strengths, explaining why the CO₂/N₂ selectivity of the modified material far exceeds that of the pristine Ni-MOF-74.

4. Conclusion

In summary, this study successfully incorporated four triazole derivatives into the Ni-MOF-74 framework, resulting in modified powders with significantly enhanced CO₂ adsorption capacity and gas separation selectivity compared to the pristine material. The overall performance followed the order: Ni-Datz-MOF-74 > Ni-Atz-MOF-74 > Ni-Mtz-MOF-74 ≈ Ni-Dmtz-MOF-74 > Ni-MOF-74. Notably, Ni-Datz-MOF-74 achieved a remarkable CO₂ adsorption capacity of 7.76 mmol g⁻¹ at 298 K (1 bar), 1.73 times that of the Ni-MOF-74. DFT calculations revealed the critical role of secondary adsorption sites (amino groups) in enhancing CO₂ adsorption. Ni-Datz-MOF-74 ranks among the top-performing MOFs in terms of adsorption capacity and exhibits balanced separation selectivity (both static and dynamic). In mixed-gas breakthrough

experiments (298 K, 15 %CO₂/85 %N₂, v/v), Ni-Datz-MOF-74 demonstrated exceptional dynamic selectivity of 172 under dry condition, 2.6 times that of the Ni-MOF-74 (66), and maintained a higher dynamic selectivity of 87 under humid condition compared to the pristine material (56). Additionally, Ni-Datz-MOF-74 exhibited excellent cycling and hydrothermal stability, which are essential for practical applications. Future work will focus on screening and designing stable amino-functionalized ligands for incorporation into MOF frameworks, aiming to achieve ultramicro pores simultaneously and N-doping (Strong quadrupole interactions with CO₂), further advancing the development of high-performance materials for carbon capture.

CRediT authorship contribution statement

Shuo Gao: Writing – review & editing, Writing – original draft, Methodology, Formal analysis, Data curation, Conceptualization. **Wanru Feng:** Writing – review & editing, Methodology. **Junsu Jin:** Writing – review & editing, Supervision, Resources, Methodology, Funding acquisition. **Jianguo Mi:** Supervision, Funding acquisition. **Hong Meng:** Supervision.

Declaration of competing interest

The authors declare that they have no known competing financial interests or personal relationships that could have appeared to influence the work reported in this paper.

Acknowledgement

This work was supported by Joint Key Program of National Natural Science Foundation of China (U22B20147).

Data availability

Data will be made available on request.

References

- [1] S. Feng, X. Du, J. Luo, Y. Zhuang, J. Wang, Y. Wan, A review on facilitated transport membranes based on π -complexation for carbon dioxide separation, *Sep. Purif. Technol.* 309 (2023) 122972, <https://doi.org/10.1016/j.seppur.2022.122972>.
- [2] C. Chen, Y. Yu, C. He, L. Wang, H. Huang, R. Albilali, J. Cheng, Z. Hao, Efficient capture of CO₂ over ordered micro-mesoporous hybrid carbon nanosphere, *Appl. Surf. Sci.* 439 (2018) 113–121, <https://doi.org/10.1016/j.apsusc.2017.12.217>.
- [3] W. Gao, Y. Chen, Y. Niu, K. Williams, L. Cash, P.J. Perez, L. Wojtas, J. Cai, Y. Chen, S. Ma, Crystal engineering of an nbo topology metal-organic framework for chemical fixation of CO₂ under ambient conditions, *Angew. Chem. Int. Ed.* 53 (2014) 2615–2619, <https://doi.org/10.1002/anie.201309778>.
- [4] D.-Y. Du, J.-S. Qin, S.-L. Li, Z.-M. Su, Y.-Q. Lan, Recent advances in porous polyoxometalate-based metal-organic framework materials, *Chem. Soc. Rev.* 43 (2014) 4615–4632, <https://doi.org/10.1039/C3CS60404G>.
- [5] B.E.R. Snyder, A.B. Turkiewicz, H. Furukawa, M.V. Paley, E.O. Velasquez, M. N. Dods, J.R. Long, A ligand insertion mechanism for cooperative NH₃ capture in metal-organic frameworks, *Nature* 613 (2023) 287–291, <https://doi.org/10.1038/s41586-022-05409-2>.
- [6] L. Ding, A.O. Yazaydin, Hydrogen and methane storage in ultrahigh surface area Metal-Organic Frameworks, *Micropor. Mesopor. Mat.* 182 (2013) 185–190, <https://doi.org/10.1016/j.micromeso.2013.08.048>.
- [7] S. Bose, D. Sengupta, T.M. Rayder, X. Wang, K.O. Kirlikoveli, A.K. Sekizkardes, T. Islamoglu, O.K. Farha, Challenges and Opportunities: metal-organic frameworks for direct air capture, *Adv. Funct. Mater.* 34 (2024) 2307478, <https://doi.org/10.1002/adfm.202307478>.
- [8] S. Chen, X. Li, J. Duan, Y. Fu, Z. Wang, M. Zhu, N. Li, Investigation of highly efficient adsorbent based on Ni-MOF-74 in the separation of CO₂ from natural gas, *Chem. Eng. J.* 419 (2021) 129653, <https://doi.org/10.1016/j.cej.2021.129653>.
- [9] Y.-Y. Liu, P. Zhang, W.-Y. Yuan, Y. Wang, Q.-G. Zhai, Extra-high CO₂ adsorption and controllable C₂H₂/CO₂ separation regulated by the interlayer stacking in pillar-layered metal-organic frameworks, *ACS Appl. Mater. Interfaces* 16 (2024) 33451–33460, <https://doi.org/10.1021/acsami.4c04760>.
- [10] J. Liu, Y. Wang, A.I. Benin, P. Jakubczak, R.R. Willis, M.D. LeVan, CO₂/H₂O adsorption equilibrium and rates on metal-organic frameworks: HKUST-1 and Ni/DOBDC, *Langmuir* 26 (2010) 14301–14307, <https://doi.org/10.1021/la102359q>.
- [11] A.A. Voskanyan, V.G. Goncharov, N. Novendra, X. Guo, A. Navrotsky, Thermodynamics drives the stability of the MOF-74 family in water, *ACS Omega* 5 (2020) 13158–13163, <https://doi.org/10.1021/acsomega.0c01189>.
- [12] R. Serna-Guerrero, E. Da'na, A. Sayari, New insights into the interactions of CO₂ with amine-functionalized silica, *Ind. Eng. Chem. Res.* 47 (2008) 9406–9412, <https://doi.org/10.1021/ie801186g>.
- [13] J.-B. Lin, T.T.T. Nguyen, R. Vaithyanathan, J. Burner, J.M. Taylor, H. Durekova, F. Akhtar, R.K. Mah, O. Ghaffari-Nik, S. Marx, N. Fylstra, S.S. Iremonger, K. W. Dawson, P. Sarkar, P. Hovington, A. Rajendran, T.K. Woo, G.K.H. Shimizu, A scalable metal-organic framework as a durable physisorbent for carbon dioxide capture, *Science* 374 (2021) 1464–1469, <https://doi.org/10.1126/science.abi7281>.
- [14] C. Yu, Q. Ding, J. Hu, Q. Wang, X. Cui, H. Xing, Selective capture of carbon dioxide from humid gases over a wide temperature range using a robust metal-organic framework, *Chem. Eng. J.* 405 (2021) 126937, <https://doi.org/10.1016/j.cej.2020.126937>.
- [15] P.D.C. Dietzel, B. Panella, M. Hirscher, R. Blom, H. Fjellvåg, Hydrogen adsorption in a nickel based coordination polymer with open metal sites in the cylindrical cavities of the desolvated framework, *Chem. Commun.* (2006) 959, <https://doi.org/10.1039/b515434k>.
- [16] E. Haque, S.H. Jhung, Synthesis of isostructural metal-organic frameworks, CPO-27s, with ultrasound, microwave, and conventional heating: effect of synthesis methods and metal ions, *Chem. Eng. J.* 173 (2011) 866–872, <https://doi.org/10.1016/j.cej.2011.08.037>.
- [17] G.H. Albuquerque, R.C. Fitzmorris, M. Ahmadi, N. Wannenmacher, P. K. Thallapally, B.P. McGrail, G.S. Herman, Gas-liquid segmented flow microwave-assisted synthesis of MOF-74(Ni) under moderate pressures, *CrstEngComm* 17 (2015) 5502–5510, <https://doi.org/10.1039/C5CE00848D>.
- [18] H. An, W. Tian, X. Lu, H. Yuan, L. Yang, H. Zhang, H. Shen, H. Bai, Boosting the CO₂ adsorption performance by defect-rich hierarchical porous Mg-MOF-74, *Chem. Eng. J.* 469 (2023) 144052, <https://doi.org/10.1016/j.cej.2023.144052>.
- [19] N. Wang, A. Mundstock, Y. Liu, A. Huang, J. Caro, Amine-modified Mg-MOF-74/CPO-27-Mg membrane with enhanced H₂/CO₂ separation, *Chem. Eng. Sci.* 124 (2015) 27–36, <https://doi.org/10.1016/j.ces.2014.10.037>.
- [20] B.S. Caglayan, A.E. Aksulu, CO₂ adsorption on chemically modified activated carbon, J. Hazard. Mater. 252–253 (2013) 19–28, <https://doi.org/10.1016/j.jhazmat.2013.02.028>.
- [21] L. Lei, Y. Cheng, C. Chen, M. Kosari, Z. Jiang, C. He, Taming structure and modulating carbon dioxide (CO₂) adsorption isosteric heat of nickel-based metal organic framework (MOF-74(Ni)) for remarkable CO₂ capture, *J. Colloid Interface Sci.* 612 (2022) 132–145, <https://doi.org/10.1016/j.jcis.2021.12.163>.
- [22] P. Wang, Z. Cai, Highly efficient flame-retardant epoxy resin with a novel DOPO-based triazole compound: thermal stability, flame retardancy and mechanism, *Polym. Degrad. Stab.* 137 (2017) 138–150, <https://doi.org/10.1016/j.polymdegradstab.2017.01.014>.
- [23] M. Ranjbar, M.A. Taher, A. Sam, Mg-MOF-74 nanostructures: facile synthesis and characterization with aid of 2,6-pyridinedicarboxylic acid ammonium, *J. Mater. Sci. Mater. Electron.* 27 (2016) 1449–1456, <https://doi.org/10.1007/s10854-015-3910-6>.
- [24] C. Chen, X. Feng, Q. Zhu, R. Dong, R. Yang, Y. Cheng, C. He, Microwave-assisted rapid synthesis of well-shaped MOF-74 (Ni) for CO₂ efficient capture, *Inorg. Chem.* 58 (2019) 2717–2728, <https://doi.org/10.1021/acs.inorgchem.8b03271>.
- [25] Y. Yue, Z.-A. Qiao, P.F. Fulvio, A.J. Binder, C. Tian, J. Chen, K.M. Nelson, X. Zhu, S. Dai, Template-free synthesis of hierarchical porous metal-organic frameworks, *J. Am. Chem. Soc.* 135 (2013) 9572–9575, <https://doi.org/10.1021/ja402694f>.
- [26] M. Sevilla, J.B. Parra, A.B. Fuertes, Assessment of the role of micropore size and N-doping in CO₂ capture by porous carbons, *ACS Appl. Mater. Interfaces* 5 (2013) 6360–6368, <https://doi.org/10.1021/am401423b>.
- [27] Y. Han, Y. Jiang, J. Hu, L. Wang, Y. Zhang, Efficient C₂H₂/CO₂ and C₂H₂/C₂H₄ separations in a novel fluorinated metal-organic framework, *Sep. Purif. Technol.* 332 (2024) 125777, <https://doi.org/10.1016/j.seppur.2023.125777>.
- [28] Y. Zhang, W. Sun, B. Luan, J. Li, D. Luo, Y. Jiang, L. Wang, B. Chen, Topological design of unprecedented metal-organic frameworks featuring multiple anion functionalities and hierarchical porosity for benchmark acetylene separation, *Angew. Chem. Int. Ed.* 135 (2023) e202309925, <https://doi.org/10.1002/ange.202309925>.
- [29] Y. Hu, L. Wang, R. Nan, N. Xu, Y. Jiang, D. Wang, T. Yan, D. Liu, Y. Zhang, B. Chen, Pore engineering in cost-effective and stable Al-MOFs for efficient capture of the greenhouse gas SF₆, *Chem. Eng. J.* 471 (2023) 144851, <https://doi.org/10.1016/j.cej.2023.144851>.
- [30] M. Sun, Y. Zhou, T. Yu, Synthesis of g-C₃N₄/NiO-carbon microsphere composites for Co-reduction of CO₂ by photocatalytic hydrogen production from water decomposition, *J. Cleaner Prod.* 357 (2022) 131801, <https://doi.org/10.1016/j.jclepro.2022.131801>.
- [31] Y. Li, X. Xu, Z. Ai, B. Zhang, D. Shi, M. Yang, H. Hu, Y. Shao, Y. Wu, X. Hao, Enhancing electrocatalytic kinetics via synergy of Co nanoparticles and Co/Ni-N₄C- and N-doped porous carbon, *ACS Appl. Mater. Interfaces* 16 (2024) 27224–27229, <https://doi.org/10.1021/acsami.4c00084>.
- [32] Q. Han, M. Shi, Z. Han, Y. Li, W. Zhang, X. Zhang, Bio-mesopores structure functional composites by mushroom-derived carbon/NiO for lithium-ion batteries, *J. Alloys Compd.* 848 (2020) 156477, <https://doi.org/10.1016/j.jallcom.2020.156477>.
- [33] J. Cui, M. Daboczi, Z. Cui, M. Gong, J. Flitcroft, J. Skelton, S.C. Parker, S. Eslava, BiVO₄ photoanodes enhanced with metal phosphide Co-catalysts: relevant properties to boost photoanode performance, *Small* 20 (2024) 2306757, <https://doi.org/10.1002/smll.202306757>.
- [34] S. Xu, M. Li, Z. Li, M. Ding, Y. Wang, Z. Jin, Coal-based carbon quantum dots modified Ni-MOF and Co/Zr-MOF heterojunctions for efficient photocatalytic hydrogen evolution, *Int. J. Hydrogen Energy* 70 (2024) 666–676, <https://doi.org/10.1016/j.ijhydene.2024.05.235>.
- [35] P. Ding, H. Song, J. Chang, S. Lu, N-doped carbon dots coupled NiFe-LDH hybrids for robust electrocatalytic alkaline water and seawater oxidation, *Nano Res.* 15 (2022) 7063–7070, <https://doi.org/10.1007/s12274-022-43774>.
- [36] H. Zhang, T. Tang, H. Wang, H. Wang, Y. Cao, H. Yu, Topological conversion of nickel foams to monolithic single-atom catalysts, *Adv. Funct. Mater.* 34 (2024) 2312939, <https://doi.org/10.1002/adfm.202312939>.
- [37] S. Zhao, Y. Cheng, J.-P. Veder, B. Johannessen, M. Saunders, L. Zhang, C. Liu, M. F. Chisholm, R. De Marco, J. Liu, S.-Z. Yang, S.P. Jiang, One-pot pyrolysis method to fabricate carbon nanotube supported Ni single-atom catalysts with ultrahigh loading, *ACS Appl. Energy Mater.* (2018) 8B00903, <https://doi.org/10.1021/acsam.8B00903>.
- [38] S. Megala, M. Sathish, S. Harish, M. Navaneethan, S. Sohila, B. Liang, R. Ramesh, Enhancement of photocatalytic H₂ evolution from water splitting by construction of two dimensional g-C₃N₄/NiAl layered double hydroxides, *Appl. Surf. Sci.* 509 (2020) 144656, <https://doi.org/10.1016/j.apsusc.2019.144656>.
- [39] J.-R. Li, R.J. Kuppler, H.-C. Zhou, Selective gas adsorption and separation in metal-organic frameworks, *Chem. Soc. Rev.* 38 (2009) 1477, <https://doi.org/10.1039/b802426j>.
- [40] Y.-M. Gu, Y.-H. Wang, S.-S. Zhao, H.-J. Fan, X.-W. Liu, Z. Lai, S.-D. Wang, N-donating and water-resistant Zn-carboxylate frameworks for humid carbon dioxide capture from flue gas, *Fuel* 336 (2023) 126793, <https://doi.org/10.1016/j.fuel.2022.126793>.
- [41] Y.-M. Gu, H.-F. Qi, T.-T. Sun, X.-W. Liu, S. Qadir, T.-J. Sun, D.-F. Li, S.-S. Zhao, D. Fairen-Jimenez, S.-D. Wang, Insights into the Ultra-high volumetric capacity in

- a robust metal–organic framework for efficient C₂H₂/CO₂ separation, *Chem. Mater.* 34 (2022) 2708–2716, <https://doi.org/10.1021/acs.chemmater.1c04168>.
- [42] Y. Hu, Y. Chen, W. Yang, J. Hu, X. Li, L. Wang, Y. Zhang, Efficient carbon dioxide capture from flue gas and natural gas by a robust metal–organic framework with record selectivity and excellent granulation performance, *Sep. Purif. Technol.* 343 (2024) 127099, <https://doi.org/10.1016/j.seppur.2024.127099>.
- [43] K. Klemenčič, A. Krajnc, A. Puškarík, M. Hus, D. Marinič, B. Likozar, N.Z. Logar, M. Mazaj, Amine-functionalized triazolate-based metal–organic frameworks for enhanced diluted CO₂ capture performance, *Angew. Chem.* 137 (2025) e202424747, <https://doi.org/10.1002/ange.202424747>.
- [44] Y.-Z. Li, G.-D. Wang, S. Lu, F. Xu, H. Zhang, Y. Sui, L. Hou, A moisture stable metal–organic framework for highly efficient CO₂/N₂, CO₂/CH₄ and CO₂/CO separation, *Chem. Eng. J.* 484 (2024) 149494, <https://doi.org/10.1016/j.cej.2024.149494>.
- [45] H. Zeng, M. Xie, Y. Huang, Y. Zhao, X. Xie, J. Bai, M. Wan, R. Krishna, W. Lu, D. Li, Induced Fit of C₂H₂ in a flexible MOF through cooperative action of open metal sites, *Angew. Chem. Int. Ed.* 58 (2019) 8515–8519, <https://doi.org/10.1002/anie.201904160>.
- [46] W. Feng, J. Zhang, J. Mi, J. Jin, G. Xiang, H. Meng, S. Xu, Efficient and selective CO₂ capture at low concentration from CH₄ or N₂ using Zn-MOF@APP composite, *J. Cleaner Prod.* 467 (2024) 143033, <https://doi.org/10.1016/j.jclepro.2024.143033>.
- [47] M. Kandiah, M.H. Nilsen, S. Usseglio, S. Jakobsen, U. Olsbye, M. Tilset, C. Larabi, E.A. Quadrelli, F. Bonino, K.P. Lillerud, Synthesis and stability of tagged UiO-66 Zr-MOFs, *Chem. Mater.* 22 (2010) 6632–6640, <https://doi.org/10.1021/cm102601v>.
- [48] K.-J. Chen, R.-B. Lin, P.-Q. Liao, C.-T. He, J.-B. Lin, W. Xue, Y.-B. Zhang, J.-P. Zhang, X.-M. Chen, New Zn-aminotriazolate-dicarboxylate frameworks: synthesis, structures, and adsorption properties, *Cryst. Growth Des.* 13 (2013) 2118–2123, <https://doi.org/10.1021/cg400183s>.
- [49] G. Aromí, L.A. Barrios, O. Roubeau, P. Gamez, Triazoles and tetrazoles: Prime ligands to generate remarkable coordination materials, *Coord. Chem. Rev.* 255 (2011) 485–546, <https://doi.org/10.1016/j.ccr.2010.10.038>.
- [50] F. Ahmadjokani, R. Mohammadkhani, S. Ahmadipourya, A. Shokrgozar, M. Rezakzemi, H. Molavi, T.M. Aminabhavi, M. Arjmand, Superior chemical stability of UiO-66 metal–organic frameworks (MOFs) for selective dye adsorption, *Chem. Eng. J.* 399 (2020) 125346, <https://doi.org/10.1016/j.cej.2020.125346>.
- [51] Y. Zhang, L. Yang, L. Wang, S. Duttwyler, H. Xing, A microporous metal–organic framework supramolecularly assembled from a Cu^{II} dodecaborate cluster complex for selective gas separation, *Angew. Chem.* 131 (2019) 8229–8234, <https://doi.org/10.1002/ange.201903600>.
- [52] R. Banerjee, A. Phan, B. Wang, C. Knobler, H. Furukawa, M. O’Keeffe, O.M. Yaghi, High-throughput synthesis of zeolitic imidazolate frameworks and application to CO₂ capture, *Science* 319 (2008) 939–943, <https://doi.org/10.1126/science.1152516>.
- [53] E.C.N. Lopes, F.S.C. Dos Anjos, E.F.S. Vieira, A.R. Cestari, An alternative Avrami equation to evaluate kinetic parameters of the interaction of Hg(II) with thin chitosan membranes, *J. Colloid Interface Sci.* 263 (2003) 542–547, [https://doi.org/10.1016/S0021-9797\(03\)00326-6](https://doi.org/10.1016/S0021-9797(03)00326-6).
- [54] N. Álvarez-Gutiérrez, M.V. Gil, F. Rubiera, C. Pevida, Kinetics of CO₂ adsorption on cherry stone-based carbons in CO₂/CH₄ separations, *Chem. Eng. J.* 307 (2017) 249–257, <https://doi.org/10.1016/j.cej.2016.08.077>.
- [55] Y. Hu, Y. Jiang, J. Li, L. Wang, M. Steiner, R.F. Neumann, B. Luan, Y. Zhang, New-generation anion-pillared metal–organic frameworks with customized cages for highly efficient CO₂ capture, *Adv. Funct. Mater.* 33 (2023) 2213915, <https://doi.org/10.1002/adfm.202213915>.
- [56] W. Liang, P.M. Bhatt, A. Shkurenko, K. Adil, G. Mouchaham, H. Aggarwal, A. Mallick, A. Jamal, Y. Belmabkhout, M. Eddaoudi, A tailor-made interpenetrated MOF with exceptional carbon-capture performance from flue gas, *Chem* 5 (2019) 950–963, <https://doi.org/10.1016/j.chempr.2019.02.007>.
- [57] Y. Jiao, Z. Du, Q. Xie, X. Wen, W. Zhang, J. Zhu, G. Lu, G. Zhou, Z. Yang, Y. Xia, Study on gas adsorption and separation performance of alkyl functionalized MOF materials under wet conditions, *RSC Adv.* 15 (2025) 2608–2617, <https://doi.org/10.1039/D4RA08720H>.
- [58] A.K. Adhikari, K.-S. Lin, Improving CO₂ adsorption capacities and CO₂/N₂ separation efficiencies of MOF-74(Ni, Co) by doping palladium-containing activated carbon, *Chem. Eng. J.* 284 (2016) 1348–1360, <https://doi.org/10.1016/j.cej.2015.09.086>.
- [59] D. Lv, J. Chen, K. Yang, H. Wu, Y. Chen, C. Duan, Y. Wu, J. Xiao, H. Xi, Z. Li, Q. Xia, Ultrahigh CO₂/CH₄ and CO₂/N₂ adsorption selectivities on a cost-effectively L-aspartic acid based metal–organic framework, *Chem. Eng. J.* 375 (2019) 122074, <https://doi.org/10.1016/j.cej.2019.122074>.
- [60] A. Justin, J. Espin, M.J. Pougin, D. Stoian, T. Schertenleib, M. Mensi, I. Kochetygov, A. Ortega-Guerrero, W.L. Queen, Post-synthetic covalent grafting of amines to NH₂-MOF for post-combustion carbon capture, *Adv. Funct. Mater.* 34 (2024) 2307430, <https://doi.org/10.1002/adfm.202307430>.
- [61] A. Sayari, Y. Belmabkhout, Stabilization of amine-containing CO₂ adsorbents: dramatic effect of water vapor, *J. Am. Chem. Soc.* 132 (2010) 6312–6314, <https://doi.org/10.1021/ja1013773>.
- [62] Y. Hu, Z. Liu, J. Xu, Y. Huang, Y. Song, Evidence of pressure enhanced CO₂ storage in ZIF-8 probed by FTIR spectroscopy, *J. Am. Chem. Soc.* 135 (2013) 9287–9290, <https://doi.org/10.1021/ja403635b>.
- [63] P. Hu, J. Hu, M. Zhu, C. Xiong, R. Krishna, D. Zhao, H. Ji, Induced-fit-identification in a rigid metal–organic framework for ppm-level CO₂ removal and ultra-pure CO enrichment, *Angew. Chem. Int. Ed.* 62 (2023) e202305944, <https://doi.org/10.1002/anie.202305944>.
- [64] K. Bhattacharyya, A. Danon, B.K. Vijayan, K.A. Gray, P.C. Stair, E. Weitz, Role of the surface Lewis acid and base sites in the Adsorption of CO₂ on Titania nanotubes and platinized titania nanotubes: an in situ FT-IR study, *J. Phys. Chem. C* 117 (2013) 12661–12678, <https://doi.org/10.1021/jp402979m>.
- [65] S.A. Didas, M.A. Sakwa-Novak, G.S. Foo, C. Sievers, C.W. Jones, Effect of amine surface coverage on the co-adsorption of CO₂ and water: spectral deconvolution of adsorbed species, *J. Phys. Chem. Lett.* 5 (2014) 4194–4200, <https://doi.org/10.1021/jz502032c>.
- [66] Y. Shi, Y. Xie, H. Cui, Z.A. Alothman, O. Alduhaisi, R.-B. Lin, B. Chen, An ultramicroporous metal–organic framework with dual functionalities for high sieving separation of CO₂ from CH₄ and N₂, *Chem. Eng. J.* 446 (2022) 137101, <https://doi.org/10.1016/j.cej.2022.137101>.
- [67] Y.-M. Gu, H.-F. Qi, S. Qadir, T.-J. Sun, R. Wei, S.-S. Zhao, X.-W. Liu, Z. Lai, S.-D. Wang, A two-dimensional stacked metal–organic framework for ultra-highly-efficient CO₂ sieving, *Chem. Eng. J.* 449 (2022) 137768, <https://doi.org/10.1016/j.cej.2022.137768>.
- [68] B. Wang, A.P. Côté, H. Furukawa, M. O’Keeffe, O.M. Yaghi, Colossal cages in zeolitic imidazolate frameworks as selective carbon dioxide reservoirs, *Nature* 453 (2008) 207–211, <https://doi.org/10.1038/nature06900>.